International Journal of Solids and Structures 208–209 (2021) 119–132

Contents lists available at ScienceDirect

International Journal of Solids and Structures

journal homepage: www.elsevier.com/locate/ijsolstr

A microstructural-based approach to model magneto-viscoelastic materials at finite strains

Daniel Garcia-Gonzalez [a,*], Mokarram Hossain [b,*]

[a] Department of Continuum Mechanics and Structural Analysis, University Carlos III of Madrid, Avda. de la Universidad 30, 28911 Leganés, Madrid, Spain
[b] Zienkiewicz Centre for Computational Engineering, College of Engineering, Swansea University, SA1 8EN, United Kingdom

ARTICLE INFO

Article history:
Received 30 April 2020
Received in revised form 30 August 2020
Accepted 29 October 2020
Available online 3 November 2020

Keywords:
Magneto-active polymers (MAP)
Magneto-mechanics
Lattice model
Magneto-viscoelasticity
Microstructural model
Finite deformations

ABSTRACT

Magneto-active polymers (MAPs) consist of a polymeric matrix filled with magnetisable particles. MAPs may change their mechanical properties (i.e., stiffness) and/or mechanical deformation upon the application of an external magnetic stimulus. Mechanical responses of MAPs can be understood as the combined contributions of both polymeric matrix and magnetic particles. Moreover, the magnetic response is defined by the interaction between magnetisable particles and the external field. Common approaches to model MAPs are based on phenomenological continuum models, which are able to predict their magneto-mechanical behaviour but sometimes failed to illustrate specific features of the underlying physics. To better understand the magneto-mechanical responses of MAPs and guide their design and manufacturing processes, this contribution presents a novel continuum constitutive model originated from a microstructural basis. The model is formulated within a finite deformation framework and accounts for viscous (rate) dependences and magneto-mechanical coupling. After the formulations, the model is calibrated with a set of experimental data. The model is validated with a wide range of experimental data that show its predictability. Such a microstructurally-motivated finite strain model will help in designing MAPs with complex three-dimensional microstructures.

1. Introduction

Magneto-active polymers (MAP) belong to a class of recently emerged advanced multi-functional materials. MAPs' mechanical and rheological properties such as elastic and shear moduli can be tuned by the application of an external magnetic stimulus. One of the most salient features of MAPs is that they can crawl, jump, move by changing their size and shape upon excitation from a remote-controlled magnetic field. These unparalleled properties make them as favourable candidates in recently emerged contactless soft robotics (Hu et al., 2018; Ren et al., 2019). In preparing a MAP, ferromagnetic (iron) particles in the size of several micrometres (microns) are dispersed in a magnetically inert polymeric matrix during the cross-linking (curing) process. Ideally, two types of MAPs can be manufactured depending on the time of application of the magnetic field during the curing process. Firstly, after mixing the iron particles in a pool of liquid monomers, the mixture can be placed to rest for chemical reactions with time. This process will result in a MAP composite where it can usually be assumed that ferromagnetic particles are more or less homogeneously distributed and locked in the polymeric matrix. Secondly, if a magnetic field is applied during the curing process, where iron particles can freely move in the pool of liquid monomers that align them in a particular direction, the mixture will produce a MAP with a preferred direction, e.g., an anisotropic composite. Recently, these smart materials have gained unprecedented importance thanks to their applications in many areas where traditional smart materials are not suitable. Some promising applications of MAPs include remote-controlled soft robotics, smart vibration absorbers, base isolation in seismic devices, tuneable stiffness actuators, soft and flexible electronics, automotive suspension bushing, sensing devices, to mention a few (Böse, 2007; Bednarek, 1999; Bellan and Bossis, 2002; Bica, 2012; Boczkowska and Awietjan, 2009; Boczkowska and Awietjan, 2012; Ginder et al., 1999, 2000, 2001; Hu et al., 2018; Ren et al., 2019; Varga et al., 2006).

Similar to numerous potential applications, experimental investigations of MAPs featuring various aspects of their mechanical and rheological characteristics have gained significant attention in the research community. These characterisation experiments include uniaxial and equi-biaxial tensile tests, compression tests, and pure shear tests under magneto-mechanical coupled loads

* Corresponding authors.
E-mail addresses: danigarc@ing.uc3m.es (D. Garcia-Gonzalez), mokarram.hossain@swansea.ac.uk (M. Hossain).

https://doi.org/10.1016/j.ijsolstr.2020.10.028
0020-7683/

(Gordaninejad et al., 2012; Kallio, 2005; Schubert and Harrison, 2015,; Stepanov et al., 2007). For most of the cases, a magnetic device is developed using either electromagnets or permanent magnets and is equipped with a traditional testing machine. For tensile experiments, strains up to 100% in MAPs under a magneto-mechanical load have been reported in the literature (Stepanov et al., 2007). However, for a very high stretching of MAP samples, the so-called magneto-rheological effects (MR) will become less pronounced. This is because the distances between magnetic particles are increased when a MAP sample is stretched largely. Among others, Kallio (2005) conducted a static compression test, where a strain level of 6.5% is applied along with a magnetic flux density up to 1.0T (Tesla). Furthermore, Gordaninejad et al. (2012) performed compressive tests up to a 20% mechanical strain under a magneto-mechanical load to quantify the MR effects on the compressive modulus. Both stress and modulus versus strain at various magnetic flux densities are used to report the compressive behavior of MAPs. Similar to uniaxial tension/compression tests, the shear mode of deformation is one of the most widely used experimental techniques to characterize the magneto-mechanical properties of polymers. However, the strain level cannot be as high as that of tensile tests. One of the key experimental studies for the shear deformation is due to Schubert and Harrison (2015), where it is depicted that the MR effect is higher at smaller strain levels and decreased with the increasing strains. They further did experiments using an equi-biaxial mode of deformation for both isotropic and anisotropic MAPs (Schubert and Harrison, 2015,). For an exhaustive review on experimental characterizations of magneto-active polymers, the recent work of Bastola and Hossain (2020) can be consulted.

MAPs and their other variants, such as magneto-active gels, magneto-active fluids etc, receive significant importance in recent years (Bosnjak et al., 2020; Garcia-Gonzalez and Landis, 2020; Kim et al., 2018; Lu et al., 2019). However, the mathematical foundations of the magneto-mechanically coupled phenomena in geometrically nonlinear settings have been established half a century ago. In this case, some of the seminal theoretical works in magneto-mechanics are due to Pao (1978), Eringen and Maugin (1990), and Maugin (1988). Similar to practical applications of MAPs, their constitutive modelling is also an active field of research. In a broad sense, we can divide the constitutive modelling approaches for MAPs into two main categories, namely i) continuum-based material models that are mostly based on phenomenological concepts, and ii) micro-mechanical constitutive formulations that are taking microscale information of the composites into account. For the first category, some of the earliest works are due to Brigadnov and Dorfmann (2003), Dorfmann and Ogden (2004a,b). In addition to constitutive laws at finite strains, they analytically solved some classical non-homogeneous boundary value problems to demonstrate the effects of a magnetic field. Despite their pioneering works in the area, they mainly concentrated on the modelling isotropic nature of the MAP composites. Bustamante (2010) and Shariff et al. (2016) developed constitutive frameworks for magneto-mechanics taking into account the underlying transverse isotropy for MAPs. Moreover, Bustamante et al. (2008), Haldar et al. (2016) provided variational formulations for magneto-mechanical balance equations that are prerequisites for the finite element solutions (FEM) of the governing equations. Note that the non-magnetic polymeric matrix in a MAP composite is a typical viscoelastic material that shows time-dependent behaviour such as strain rate-dependence, stress relaxation or creeps. However, the aforementioned pioneering works did not consider the time-dependence behaviour of MAPs. Very recently, Saxena et al. (2013, 2014) and Nedjar (2019) proposed constitutive frameworks that consider time-dependent viscoelastic behaviour of the so-called soft MAPs (Zhao et al., 2019), while Garcia-Gonzalez (2019) devised a computational framework for simulating time-dependent behaviour of hard magneto-materials. These time-dependent responses were also incorporated in the constitutive formulation of magneto-active hydrogels to study their effects across different time scales by Garcia-Gonzalez and Landis (2020).

One of the main limitations of the continuum-based models is that they do not contain any detailed information of the microstructures for MAP composites. For instance, they do not provide any explicit information on how the ferromagnetic particles are arranged inside the non-magnetic matrices. Hence, such models loosely classify MAPs into two groups, isotropic if particles are randomly dispersed and anisotropic when iron fillers are aligned in a chain-like structure. However, experimental evidences demonstrated that particles are arranged in more complex distributions rather than the two particular structures as assumed in the continuum-based finite strain constitutive models. Therefore, micromechanics-inspired constitutive laws gain popularity over the former one as the latter class of models explicitly inhibit the information on how the particles are enclosed into the polymeric matrix. Primarily, this modelling approach considers magnetic interactions between embedded magnetic fillers and their corresponding effects on the polymeric matrix which are the main reasons behind the change of properties under an applied magnetic field. Among others, the so-called lattice model is a successful technique to explain various phenomena observed in a MAP. One of the earliest one-dimensional lattice model is due to Jolly et al. (1996). The lattice model of Jolly et al. (1996) is extended and rigorously studied by Ivaneyko et al. (2011, 2012, 2014) in a series of papers. They successfully predicted various stiffness (e.g., shear and elastic moduli) gaining phenomena and contraction and expansion mechanisms of MAP composites under a magnetic load. Very recently, Khanouki et al. (2019) and Gao and Wang (2019) adapted the lattice model and calibrated it under different magneto-mechanical loads with a wide range of experimental data from MAP composites.

Despite many promising features of the lattice model, to the best of the authors' knowledge, there is no finite strain version of the approach. Moreover, the current version of the lattice model does not have any clear strategy to capture the viscoelastic behaviour of MAPs. The aim of this contribution is to develop a microstructural-based magneto-mechanical constitutive model incorporating the viscoelastic phenomena, whose significance has largely been demonstrated in MAPs. To this end, firstly, the lattice model will be extended for finite strains. Secondly, the proposed framework will be further extended to account for the time-dependent viscoelastic behaviour of MAP composites. After devising the framework in a thermodynamically consistent way using the relevant laws of thermodynamics, strain energies will be derived considering the microscale information of the particle arrangements within the MAP. Subsequently, the proposed model will be calibrated with some classical experimental data available in the literature. Once relevant parameters of the model will be identified and validated, microstructural flexibility of the model will be further explained.

The manuscript is divided into six Sections. In Section 2, some basic equations of magneto-mechanics at finite strains are briefly elaborated. In the same section, the total stress tensor and magnetic variables are derived from the relevant laws of thermodynamics. Section 3 elaborates the key concepts that motivate the proposed microstructural-based magneto-mechanical constitutive model at finite strains. Mechanical strain energies, magnetic strain energy and the evolution equation to track the internal variables are elaborated in this section. In Section 4, the model is calibrated with some classical experimental data. After fitting the model with a set of data, relevant parameters are identified and further validated with new sets of data. Section 5 demonstrates the flexibility

of the proposed model by considering several complex scenarios of particle arrangements within MAPs. Finally, concluding remarks close the paper in Section 6 with an outlook for future works.

2. Basic equations of magneto-mechanics for finite strains

2.1. Kinematics

Polymeric materials are highly deformable. Therefore, in defining various kinematic quantities, it is customary to differentiate between the material configuration $\mathcal{B}_0$ and the spatial configuration $\mathcal{B}_t$. In order to track the deformation of a body, a point defined in the material coordinates $\boldsymbol{X}$ in $\mathcal{B}_0$ is moved onto the spatial coordinates $\boldsymbol{x}$ in $\mathcal{B}_t$ through the nonlinear deformation map $\boldsymbol{\chi}$. Such a mapping process will help in defining the deformation gradient $\boldsymbol{F}$, one of the key quantities in nonlinear kinematics, as

$$\boldsymbol{F} = \text{Grad}\boldsymbol{\chi}; \quad J := \det \boldsymbol{F} > 0. \tag{1}$$

This definition of the deformation gradient leads to some more strain measures such as the left and the right Cauchy-Green tensors $\boldsymbol{b}$ and $\boldsymbol{C}$, respectively, as

$$\boldsymbol{b} := \boldsymbol{F}\boldsymbol{F}^T, \quad \boldsymbol{C} := \boldsymbol{F}^T\boldsymbol{F}. \tag{2}$$

In order to model the time-dependent responses for polymeric materials, one of the classical approaches in finite strain viscoelasticity is the multiplicative decomposition of the deformation gradient $\boldsymbol{F}$, where the gradient is decomposed into an elastic ($\boldsymbol{F}^e$) and a viscous ($\boldsymbol{F}^v$) contributions (Lee, 1969; Saxena et al., 2013) as

$$\boldsymbol{F} = \boldsymbol{F}^e\boldsymbol{F}^v. \tag{3}$$

The aforementioned multiplicative decomposition results in further expressions of various strain measures as $\boldsymbol{C}^e = [\boldsymbol{F}^e]^T\boldsymbol{F}^e$ and $\boldsymbol{C}^v = [\boldsymbol{F}^v]^T\boldsymbol{F}^v$. In magneto-mechanics, three main quantities are considered as the fundamental variables. These are magnetic field $\mathbb{H}$, magnetisation $\mathbb{M}$, and magnetic induction $\mathbb{B}$in the material configuration, while $\mathbb{h}, \mathbb{m}$, and $\mathbb{b}$are the same, respectively, in the spatial configuration. The three key variables in the two different configurations are related by

$$\mathbb{H} = \mathbb{h}\boldsymbol{F}, \quad \mathbb{M} = \mathbb{m}\boldsymbol{F}, \quad \mathbb{B} = J\mathbb{b}\boldsymbol{F}^{-T}. \tag{4}$$

2.2. Balance laws in material configuration

The balances for the magnetic field $\mathbb{H}$and the magnetic induction $\mathbb{B}$in magneto-mechanics are due to Maxwell equations, which, in the material configuration, are defined as

$$\text{Curl}\mathbb{H} = \boldsymbol{0}, \quad \text{Div}\mathbb{B} = 0, \tag{5}$$

where, Curl and Div denote the corresponding differential operators with respect to the position vectors $\boldsymbol{X}$ in $\mathcal{B}_0$. Note that if we derive $\mathbb{H}$ from a scalar potential φ, equation $(5)_1$ will automatically be satisfied, i.e.,

$$\mathbb{H} = -\text{Grad}\varphi, \quad \text{in}\mathcal{B}_0. \tag{6}$$

In the bulk $\mathbb{B}$, $\mathbb{H}$ and $\mathbb{M}$ are connected by the relation, cf. Dorfmann and Ogden (2004a) and Mehnert et al. (2017)

$$\mathbb{B} = J\mu_0\boldsymbol{C}^{-1}[\mathbb{H} + \mathbb{M}] \quad \text{in}\mathcal{B}_0. \tag{7}$$

Sometimes, it is more convenient to express stresses either in the form of total Cauchy stress $\boldsymbol{\sigma}^{\text{tot}}$ defined in the spatial configuration or in the form of total second Piola–Kirchhoff stress $\boldsymbol{S}^{\text{tot}}$ defined in the material configuration. These are related to the total first Piola–Kirchhoff stress tensor $\boldsymbol{P}^{\text{tot}}$ via

$$\boldsymbol{P}^{\text{tot}} = J\boldsymbol{\sigma}^{\text{tot}}\boldsymbol{F}^{-T}, \quad \boldsymbol{S}^{\text{tot}} = J\boldsymbol{F}^{-1}\boldsymbol{\sigma}^{\text{tot}}\boldsymbol{F}^{-T}. \tag{8}$$

The total Piola stress contains the contributions from the mechanical ($\boldsymbol{P}$) as well as the ponderomotive parts ($\boldsymbol{P}^{\text{pon}}$). Hence, it is decomposed into

$$\boldsymbol{P}^{\text{tot}} = \boldsymbol{P} + \boldsymbol{P}^{\text{pon}} = \boldsymbol{P} + \boldsymbol{P}^{\text{mag}} + \boldsymbol{P}^{\text{max}}, \tag{9}$$

with the magnetization Piola stress $\boldsymbol{P}^{\text{mag}}$ and the Maxwell Piola stress $\boldsymbol{P}^{\text{max}}$ that can be expressed as

$$\boldsymbol{P}^{\text{mag}} = [\mathbb{M}\cdot\mathbb{B}]\boldsymbol{F}^{-T} - \mathbb{m}\otimes\mathbb{B}, \quad \text{and}$$
$$\boldsymbol{P}^{\text{max}} = -M_0\boldsymbol{F}^{-T} + \frac{1}{\mu_0}\mathbb{b}\otimes\mathbb{B}. \tag{10}$$

In Eq. (10) $M_0 = \frac{1}{2\mu_0}J^{-1}\mathbb{B}\cdot[\boldsymbol{C}\mathbb{B}]$ denotes the magneto-static energy density per unit volume in the material configuration.

2.3. Constitutive equations

In isothermal case, the strain energy function (per unit volume) of a magneto-viscoelastic material can be expressed as a function of the deformation gradient ($\boldsymbol{F}$), an internal variable ($\boldsymbol{F}^v$), and a magnetic variable ($\mathbb{M}$) as

$$\Psi = \tilde{\Psi}(\boldsymbol{F}, \boldsymbol{F}^v, \mathbb{M}). \tag{11}$$

Note that the strain energy function might depend on any of the three independent (primary) magnetic variables, $\mathbb{H}$, $\mathbb{M}$, and $\mathbb{B}$, see Dorfmann and Ogden (2004a,b) for more details. The concept of the total energy function is a widely-known modelling approach in magneto-mechanics, where the total energy is expressed as

$$\Omega(\boldsymbol{F}, \boldsymbol{F}^v, \mathbb{M}) = \Psi(\boldsymbol{F}, \boldsymbol{F}^v, \mathbb{M}) + M_0^*(\boldsymbol{F}, \mathbb{M}), \tag{12}$$

and $M_0^*(\boldsymbol{F}, \mathbb{M}) := -\frac{1}{2}J\mu_0\mathbb{H}\cdot[\boldsymbol{C}^{-1}\mathbb{H}]$ is called the free field magnetic energy in the material configuration. In the case of isothermal loading, the second law of thermodynamics in the form of the Clausius–Duhem inequality will become (Coleman and Gurtin, 1967; Maugin, 1988)

$$\delta_0 = \boldsymbol{P}^{\text{tot}} : \dot{\boldsymbol{F}} + p\boldsymbol{F}^{-T} : \dot{\boldsymbol{F}} + \mathbb{B}\cdot\dot{\mathbb{M}} - \dot{\Omega} \geqslant 0, \tag{13}$$
$$= \boldsymbol{P}^{\text{tot}} : \dot{\boldsymbol{F}} + p\boldsymbol{F}^{-T} : \dot{\boldsymbol{F}} + \mathbb{B}\cdot\dot{\mathbb{M}} - \frac{\partial\Omega}{\partial\boldsymbol{F}} : \dot{\boldsymbol{F}} - \frac{\partial\Omega}{\partial\boldsymbol{F}_v} : \dot{\boldsymbol{F}}_v - \frac{\partial\Omega}{\partial\mathbb{M}} : \dot{\mathbb{M}} \geqslant 0. \tag{14}$$

Note that the term related to p (a Lagrange multiplier) is inserted here to impose the incompressibility constraint frequently used for modelling rubber-like materials (Kadapa and Hossain, 2020; de Souza Neto et al., 2008). Now, with the help of Coleman-Noll argumentation (Coleman and Gurtin, 1967), we can express the constitutive relations in terms of the total energy as

$$\boldsymbol{P}^{\text{tot}} = -p\boldsymbol{F}^{-T} + \frac{\partial\Omega}{\partial\boldsymbol{F}}, \quad \text{with} \quad \boldsymbol{P}^{\text{max}} = \frac{\partial M_0^*}{\partial\boldsymbol{F}}, \quad \mathbb{B} = \frac{\partial\Omega}{\partial\mathbb{M}}. \tag{15}$$

The remaining term $-\frac{\partial\Omega}{\partial\boldsymbol{F}_v} : \dot{\boldsymbol{F}}_v \geqslant 0$ will be used to find an evolution equation for $\boldsymbol{F}_v$ in the following section. For more details on fundamental equations of magneto-mechanics, readers are referred to our recent publications (Hossain et al., 2015a,b,c; Garcia-Gonzalez, 2019) and also in some classical text books such as Griffiths (1998), Kovetz (2000) and Brown (1966).

3. A microstructural-based magneto-viscoelastic model

This section presents the key concepts that we use here to develop a microstructural-based energy function in pursuing a magneto-mechanically coupled constitutive law at finite strains.

Afterwards, the corresponding stress tensors will be derived from the energy functions. Finally, constitutive equations for magnetisation and viscous flow rule are defined.

3.1. Conceptualisation of the constitutive model

A MAP is a composite material consisting of a largely deformable polymeric matrix and a small portion of soft-magnetic particles which are responsive to an external magnetic field. The matrix part is assumed as a non-linear viscoelastic polymer whose mechanical responses can be understood as the combination of purely hyperelastic and rate dependent (viscous) components. The magnetic particles are considerably stiffer than the polymeric matrix so, apart from incorporating the magnetostrictive response to the composite, the particles influence the overall mechanical stiffness of the MAP. Several experimental studies reveal that when particles are randomly oriented (isotropic case), an external magnetic field can expand a MAP sample as well as the field will enhance the elastic modulus (Bellan and Bossis, 2002; Diguet et al., 2010; Zhou and Jiang, 2004), which are consistent with some theoretical works that are mainly based on continuum mechanical approaches (Dorfmann and Ogden, 2004b; Borcea and Bruno, 2001). On the contrary, some theoretical works predict sample contractions and reductions in elastic moduli for MAPs of homogeneously distributed particles (isotropic MAPs) (Kankanala and Triantafyllidis, 2004; Ivaneyko et al., 2011; Martin et al., 2006).

In the case of chain-like distributions of the magnetic particles (anisotropic case), upon application of the magnetic field, a MAP sample will either expand or contract and the elastic modulus will increase, see Coquelle and Bossis (2005), Jolly et al. (1996) and Zhou and Jiang (2004). Based on these experimental findings, Ivaneyko et al. (2011) developed a lattice model to capture some key features observed in the MAPs. Despite the initial success, the model fails to predict elastic stiffness gaining and the sample expansion in the case of homogeneously distributed (isotropic) and chain-like anisotropic arrangement of particles. This is because in their earliest version of the lattice model, iron particles are assumed to be placed in a simple cubic (SC) lattice. They rectified the model by considering the arrangement of particles in more complex lattices such as body-centred cubic (BCC) lattice and hexagonal closed-packed (HCP) lattice (Ivaneyko et al., 2012, 2014). Han et al. (2013) further modified the lattice model by adding a 'wavy factor' that represents a magnitude of how well-aligned the particles are. Thus, the magnetostrictive response of the MAP is observed to change from a contraction to an elongation when varying the wavy factor. The approach assumes that a tensile deformation of wavy chains is mainly due to an effective shear deformation of irregular (wavy) chains, in turn resulting into the increase of the stiffness under the application of a magnetic field.

In an effort to develop a microstructural-based magneto-viscoelastic model, we depart from the classical lattice model. In this case, we provide a more generic distribution of the magnetic particles by considering it into three main groups: isotropic distribution, perfectly aligned distribution, and wavy chain distribution, see Fig. 1. When a MAP is subjected to a magneto-mechanical loading, it has strain energy per unit reference volume, Ψ, that can be decomposed into a mechanical and a magnetic parts Ψ_{m} and Ψ_{mg}, respectively:

$$\Psi(\boldsymbol{F}, \boldsymbol{F}^{v}, \mathbb{M}) = \Psi_{\mathrm{m}}(\boldsymbol{F}, \boldsymbol{F}^{v}) + \Psi_{\mathrm{mg}}(\boldsymbol{F}, \mathbb{M}). \tag{16}$$

In addition, the mechanical contribution is conceived as the sum of a purely elastic component Ψ^{e}_{m}, associated to the magnetic particles and polymeric matrix, and a viscoelastic component Ψ^{v}_{m} associated to relaxation processes within the polymeric matrix. Therefore, the mechanical contribution to the strain energy can be defined as:

$$\Psi_{\mathrm{m}}(\boldsymbol{F}, \boldsymbol{F}^{v}) = \Psi^{e}_{\mathrm{m}}(\boldsymbol{F}) + \Psi^{v}_{\mathrm{m}}(\boldsymbol{F}, \boldsymbol{F}^{v}). \tag{17}$$

For the magnetic part of the energy function, we at first develop a strain energy function based on the particle arrangements at the microscale. Afterwards, it will be transferred at macroscale by an affinity assumption. A representative scheme of the model is presented in Fig. 2. As shown in the figure, the total deformation gradient allows for going from a reference configuration $\mathcal{B}_0$ to a current (or deformed) configuration $\mathcal{B}_t$. Note that this change of configuration through the deformation gradient applies to both the macro- and the microscales. The magnetic potential $\Psi_{\mathrm{mg}}(\boldsymbol{F}, \mathbb{M})$ is based on magnetic dipole–dipole interactions and can be written as a function of the magnetization variable $\mathbb{M}$ and the total deformation gradient $\boldsymbol{F}$. The latter dependence arises from the fact that the mechanical deformation alters distances between magnetic particles and, therefore, their interactions.

3.2. Strain energy functions

3.2.1. Mechanical strain energy functions

Magnetic particles are much stiffer than the polymeric matrix in a MAP. Therefore, the particles can be assumed to behave as a non-deformable solid. Both the elastic and viscous contributions are related to the polymeric part and must be associated with its volume fraction. The polymeric volume fraction is defined as $[1-\phi]$, with ϕ being the magnetic particles' volume ratio. Although the viscous properties of the MAP are not significantly influenced by the particles, an amplification factor needs to be included into the elastic contribution to model the stiffening effect of filling the polymeric matrix with the particles. The present framework provides flexibility to define the mechanical part of the energy function, without the loss of generality, depending on the specific polymeric matrix to be modelled. To illustrate the flexibility, we provide two particularisations of the mechanical energy. The first one defines both elastic and viscous contributions by a physically-motivated microstructural approach based on the 8-chain concept originally proposed by Arruda and Boyce (1993) (also known as the 8-chain model). The second strain energy function is taken from a first invariant-based model proposed by

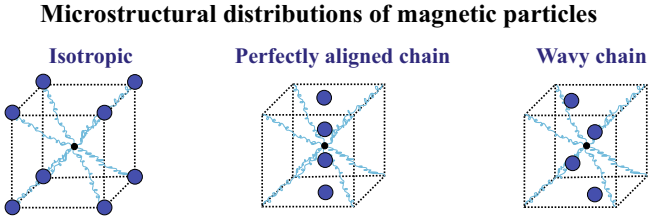

Fig. 1. Various possibilities for magnetic particles distributions considered in this work: isotropic, perfectly aligned chain, and wavy chain distributions.

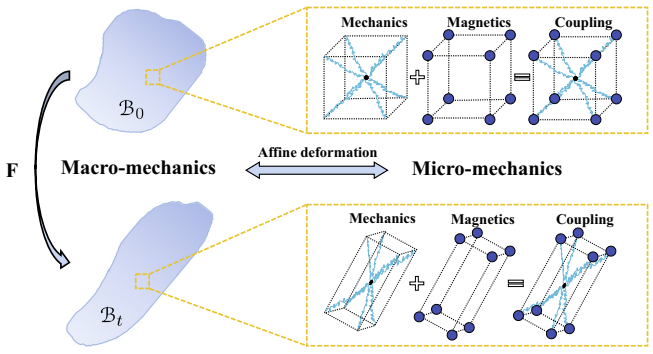

Fig. 2. A schematic diagram of the microstructural-based model showing the couplings between macro- and micro-scales and MAP physics.

Lopez-Pamies (LP) (Lopez-Pamies, 2010). The LP model is a phenomenologically-motivated strain energy function to capture specific polymeric responses. For an exhaustive review to observe advantages and limitations of different hyperelastic energy functions, Steinmann et al. (2012) can be consulted. Note that more advanced forms of micro-mechanically motivated constitutive models can be taken to capture a wide strain range spanning from very small to large. However, such an advanced model comes up with a large number of material parameters, see, for example, Refs.: Miehe et al. (2004) and Davidson and Goulbourne (2013). The elastic and viscous mechanical potentials are defined, respectively, for the 8-chain (8c) model as:

$$\begin{aligned}\Psi^{e}_{\mathrm{m,8c}}(\boldsymbol{F}) &= [1-\phi]G^{e}\sum_{k=1}^{K}\frac{C_k}{N_e^{k-1}}\left[I_{1,h}^{k}-3^{k}\right]\\ \Psi^{v}_{\mathrm{m,8c}}(\boldsymbol{F},\boldsymbol{F}^{v}) &= [1-\phi]G^{v}\sum_{k=1}^{K}\frac{C_k}{N_v^{k-1}}\left[\left[I_1^{e}\right]^{k}-3^{k}\right],\end{aligned} \tag{18}$$

where, G^e and G^v are the shear moduli for the elastic and viscous responses, respectively, N_e and N_v are the number of Kuhn segments per polymer chain for the elastic and viscous networks, respectively, and $I_1^e = \mathrm{tr}(\boldsymbol{C}^e)$. We take up to five terms in the summation, i.e., $[C_1, C_2, C_3, C_4, C_5] = \left[\frac{1}{2}, \frac{1}{20}, \frac{11}{1050}, \frac{19}{7000}, \frac{519}{673750}\right]$. Due to the particles' influences, the first invariant I_1 is modified to $I_{1,h}$, which is defined as:

$$I_{1,h} = X[I_1 - 3] + 3 \tag{19}$$

where, $I_1 = \mathrm{tr}(\boldsymbol{C})$ and X is the application factor defined as:

$$X = 1 + 0.67g\phi + 1.62[g\phi]^2 \tag{20}$$

with g being a factor describing the asymmetric nature of the aggregated clusters, see Alshammari et al. (2019) and Liao et al. (2020). The second model considered herein is due to Lopez-Pamies (LP) strain energy function as:

$$\begin{aligned}\Psi^{e}_{\mathrm{m,LP}}(\boldsymbol{F}) &= [1-\phi]\sum_{k=1}^{K}\frac{3^{1-\alpha_k^e}}{2\alpha_k^e}G_k^{e}\left[I_{1,h}^{\alpha_k^e}-3^{\alpha_k^e}\right]\\ \Psi^{v}_{\mathrm{m,LP}}(\boldsymbol{F},\boldsymbol{F}^{v}) &= [1-\phi]\sum_{k=1}^{K}\frac{3^{1-\alpha_k^v}}{2\alpha_k^v}G_k^{v}\left[\left[I_1^{e}\right]^{\alpha_k^v}-3^{\alpha_k^v}\right]\end{aligned} \tag{21}$$

where, G_k^e and α_k^e are material parameters that determine the shear modulus of the elastic response, G_k^v and α_k^v are material parameters that describe the same for the viscous response.

3.2.2. Magnetic strain energy function

The magnetic potential per unit volume is defined considering the dipole–dipole interactions of the magnetisable particles:

$$\Psi_{\mathrm{mg}}(\boldsymbol{F},\mathbb{M}) = -\frac{1}{V_0}\frac{\mu_r\mu_o}{4\pi}\sum_{ij}\left[\frac{3\left[\boldsymbol{m}_{di}\cdot\boldsymbol{r}_{ij}\right]\left[\boldsymbol{m}_{di}\cdot\boldsymbol{r}_{ij}\right]}{\|\boldsymbol{r}_{ij}\|^5} - \frac{\left[\boldsymbol{m}_{di}\cdot\boldsymbol{m}_{dj}\right]}{\|\boldsymbol{r}_{ij}\|^3}\right] \tag{22}$$

where, μ_r is the relative permeability of the medium, μ_0 is the relative permeability of the vacuum, V_0 is the reference volume of the MAP, $\boldsymbol{m}_{di}$ and $\boldsymbol{m}_{dj}$ are dipole moments $\boldsymbol{m}_{di} = \boldsymbol{m}_{dj} = v_p\mathbb{m} = v_p\boldsymbol{F}^{-T}\mathbb{M}$ of the i-th and j-th magnetic particles with v_p being the particle volume. Note that $\boldsymbol{r}_{ij}$ represents the vectorial distance between the i-th and j-th particles in the current configuration. If a homogeneous distribution of magnetic particles is assumed, a representative volume element can be chosen along with its characteristic lattice (see Fig. 1 for different distributions of magnetic particles). Following the methodology used by Ivaneyko et al. (2012), the expression for the magnetic potential can be simplified by substituting double sum over pairs of indices i and j to a sum of index i multiplied by N number of particles within a MAP. In addition, the symmetries of the infinite lattices result into the orientation of the magnetic dipoles along the external magnetic field direction ($\mathbb{H}$), and identical magnetisation for all particles. Thus, the magnetic strain energy function can be simplified as:

$$\Psi_{\mathrm{mg}}(\boldsymbol{F},\mathbb{M}) = -\frac{N v_p^2}{V_0} \times\frac{\mu_r\mu_o}{4\pi}\sum_{i=1}^{M}\left[\frac{3\left[\left[\boldsymbol{F}^{-T}\mathbb{M}\right]\cdot\boldsymbol{r}_i\right]\left[\left[\boldsymbol{F}^{-T}\mathbb{M}\right]\cdot\boldsymbol{r}_i\right]}{\|\boldsymbol{r}_i\|^5} - \frac{\left[\boldsymbol{F}^{-T}\mathbb{M}\right]\cdot\left[\boldsymbol{F}^{-T}\mathbb{M}\right]}{\|\boldsymbol{r}_i\|^3}\right]. \tag{23}$$

Note that the distances $\boldsymbol{r}_i$ will change with deformation according to:

$$\boldsymbol{r}_i = \boldsymbol{F}\boldsymbol{R}_i \tag{24}$$

where, $\boldsymbol{R}_i$ is the distance between particles in the reference configuration. For the sake of simplicity, we take an affinity assumption for the transformation from a microscale to a macroscale. This term can be written depending on the characteristic length of the lattice l_c as $\boldsymbol{R}_i = l_c\boldsymbol{R}_i^0$, with $\boldsymbol{R}_i^0$ being a dimensionless distance between particles. Note that the magnetic potential can be rewritten, for the sake of convenience, depending on the magnetic particle's volume fraction ϕ recalling the equalities $\phi = \frac{N v_p}{V_0}$ and $\phi = \frac{v_p}{l_c^3}$. Therefore, the magnetic strain energy function finally reads as:

$$\Psi_{\mathrm{mg}}(\boldsymbol{F},\mathbb{M}) = -\frac{\mu_r\mu_o}{4\pi} \times\frac{\phi^2}{\gamma}\sum_{i=1}^{N}\left[\frac{3\left[\left[\boldsymbol{F}^{-T}\mathbb{M}\right]\cdot\left[\boldsymbol{F}\boldsymbol{R}_i^0\right]\right]\left[\left[\boldsymbol{F}^{-T}\mathbb{M}\right]\cdot\left[\boldsymbol{F}\boldsymbol{R}_i^0\right]\right]}{\|\boldsymbol{F}\boldsymbol{R}_i^0\|^5} - \frac{\left[\boldsymbol{F}^{-T}\mathbb{M}\right]\cdot\left[\boldsymbol{F}^{-T}\mathbb{M}\right]}{\|\boldsymbol{F}\boldsymbol{R}_i^0\|^3}\right] \tag{25}$$

where, the term γ is added to account for the number of particles per representative lattice selected (see Ivaneyko et al., 2012 for similar approaches).

3.3. Derivation of the total stress

In order to obtain a complete expression for the total stress $\boldsymbol{P}^{\mathrm{tot}}$, three parts of the strain energy functions are required which are derived in the previous sections. The vacuum permeability of the free space term $M_0^s(\boldsymbol{F},\mathbb{M})$ in the total energy formulation has negligible effects as mentioned in the literature (Mehnert et al., 2017). Hence, in this sequel $\Omega(\boldsymbol{F},\boldsymbol{F}^v,\mathbb{M}) \approx \Psi(\boldsymbol{F},\boldsymbol{F}^v,\mathbb{M})$ will be approximated onwards. Using the definition in Eq. (15), the total first Piola–Kirchhoff stress tensor becomes

$$\boldsymbol{P}^{\mathrm{tot}} = -p\boldsymbol{F}^{-T} + \frac{\partial\Psi}{\partial\boldsymbol{F}} \tag{26}$$

which can be further decomposed into several stress tensor parts:

$$\begin{aligned}\boldsymbol{P}^{\mathrm{tot}} &= -p\boldsymbol{F}^{-T} + \frac{\partial\Psi^{e}_{\mathrm{m}}}{\partial\boldsymbol{F}} + \frac{\partial\Psi^{v}_{\mathrm{m}}}{\partial\boldsymbol{F}^{e}}\boldsymbol{F}^{-v} + \frac{\partial\Psi_{\mathrm{mg}}}{\partial\boldsymbol{F}}\\ &= -p\boldsymbol{F}^{-T} + \boldsymbol{P}^{e}_{\mathrm{m}} + \boldsymbol{P}^{v}_{\mathrm{m}} + \boldsymbol{P}_{\mathrm{mg}}.\end{aligned} \tag{27}$$

In the aforementioned equation, $\boldsymbol{P}^{e}_{\mathrm{m}} = \frac{\partial\Psi^{e}_{\mathrm{m}}}{\partial\boldsymbol{F}}$ is the elastic component of the mechanical contribution, $\boldsymbol{P}^{v}_{\mathrm{m}} = \frac{\partial\Psi^{v}_{\mathrm{m}}}{\partial\boldsymbol{F}^{e}}\boldsymbol{F}^{-v}$ is the viscous component of the mechanical contribution and $\boldsymbol{P}_{\mathrm{mg}} = \frac{\partial\Psi_{\mathrm{mg}}}{\partial\boldsymbol{F}}$ is the magnetic contribution. For the 8-chain model, the mechanical parts (elastic and viscous parts) of the first Piola–Kirchhoff stress tensor become

$$\begin{aligned}\boldsymbol{P}^{e}_{\mathrm{m,8c}} &= [1-\phi]\left[2XG^{e}\sum_{k=1}^{K}\frac{kC_k}{N_e^{k-1}}I_{1,h}^{k-1}\right]\boldsymbol{F},\\ \boldsymbol{P}^{v}_{\mathrm{m,8c}} &= [1-\phi]\left[2G^{v}\sum_{k=1}^{K}\frac{kC_k}{N_v^{k-1}}\left[I_1^{e}\right]^{k-1}\right]\boldsymbol{F}^{e}\boldsymbol{F}^{-v}\end{aligned} \tag{28}$$

while the same for the Lopez-Pamies (LP) model become

$$\boldsymbol{P}^{e}_{\mathrm{m,LP}} = [1-\phi]\sum_{k=1}^{K} 3^{1-\alpha^{e}_{k}} G^{e}_{k} X I^{\alpha^{e}_{k}-1}_{1,h} \boldsymbol{F},$$
$$\boldsymbol{P}^{v}_{\mathrm{m,LP}} = [1-\phi]\sum_{k=1}^{K} 3^{1-\alpha^{v}_{k}} G^{v}_{k} \left[I^{e}_{1}\right]^{\alpha^{v}_{k}-1} \boldsymbol{F}^{e}\boldsymbol{F}^{-v}. \tag{29}$$

Using Eq. (25), we obtain the magnetic stress tensor as

$$\boldsymbol{P}_{mg} = -\frac{\mu_r \mu_o \phi^2}{4\pi\gamma} \times \sum_{i}\left[\frac{-6\left(\left(\boldsymbol{F}^{-\mathrm{T}}\mathbb{M}\right)\otimes\left(\boldsymbol{F}^{-\mathrm{T}}\boldsymbol{F}\boldsymbol{R}^{0}_{i}\right)\right)\left(\left(\boldsymbol{F}^{-\mathrm{T}}\mathbb{M}\right)\cdot\left(\boldsymbol{F}\boldsymbol{R}^{0}_{i}\right)\right)+6\left(\left(\boldsymbol{F}^{-\mathrm{T}}\mathbb{M}\right)\cdot\left(\boldsymbol{F}\boldsymbol{R}^{0}_{i}\right)\right)\left(\left(\boldsymbol{F}^{-\mathrm{T}}\mathbb{M}\right)\otimes\boldsymbol{R}^{0}_{i}\right)}{\|\boldsymbol{F}\boldsymbol{R}^{0}_{i}\|^{5}} - \frac{15\left(\left(\boldsymbol{F}^{-\mathrm{T}}\mathbb{M}\right)\cdot\left(\boldsymbol{F}\boldsymbol{R}^{0}_{i}\right)\right)\left(\left(\boldsymbol{F}^{-\mathrm{T}}\mathbb{M}\right)\cdot\left(\boldsymbol{F}\boldsymbol{R}^{0}_{i}\right)\right)\left(\boldsymbol{R}^{0}_{i}\otimes\boldsymbol{R}^{0}_{i}\right)\boldsymbol{F}}{\|\boldsymbol{F}\boldsymbol{R}^{0}_{i}\|^{7}} + \frac{2\left(\boldsymbol{F}^{-\mathrm{T}}\mathbb{M}\right)\otimes\left(\boldsymbol{F}^{-\mathrm{T}}\boldsymbol{F}^{-\mathrm{T}}\mathbb{M}\right)}{\|\boldsymbol{F}\boldsymbol{R}^{0}_{i}\|^{3}} - \frac{3\left(\left(\boldsymbol{F}^{-\mathrm{T}}\mathbb{M}\right)\cdot\left(\boldsymbol{F}^{-\mathrm{T}}\mathbb{M}\right)\right)\left(\boldsymbol{R}^{0}_{i}\otimes\boldsymbol{R}^{0}_{i}\right)\boldsymbol{F}}{\|\boldsymbol{F}\boldsymbol{R}^{0}_{i}\|^{5}}\right] \tag{30}$$

3.4. Constitutive equations for magnetisation and flow rule

Note that it can be convenient to use the nominal magnetic field vector as the independent magnetic variable instead of the nominal magnetisation (i.e., for FE implementation purposes). To this end and without the loss of generality, the total energy function $\Omega(\boldsymbol{F}, \boldsymbol{F}^{v}, \mathbb{M})$ can be re-written by making use of the Legendre transform ($\hat{\Omega}(\boldsymbol{F}, \boldsymbol{F}^{v}, \mathbb{B}) = \Omega(\boldsymbol{F}, \boldsymbol{F}^{v}, \mathbb{M}) - \mathbb{B}\cdot\mathbb{M}$) and Eq. (7) as $\tilde{\Omega}(\boldsymbol{F}, \boldsymbol{F}^{v}, \mathbb{H})$ (see Garcia-Gonzalez and Landis (2020) for a similar approach). Therefore, the magnetic constitutive equation from Eq. (15) thus reads as:

$$\mathbb{M} = -\frac{\partial\tilde{\Omega}}{\partial\mathbb{H}}. \tag{31}$$

To define such an evolution of the magnetisation $\mathbb{M}$ with respect to the magnetic field $\mathbb{H}$, the Froehlich-Kennely equation is used:

$$\mathbb{M} = \frac{M_s\left[\mu_r - 1\right]\mathbb{H}}{M_s + \left[\mu_r - 1\right]\|\mathbb{H}\|} \tag{32}$$

where, M_s is the saturation magnetisation of the magnetic particles and μ_r is the relative magnetic permeability of the particles (Ivaneyko et al., 2011, 2012). Now, the evolution of the viscous part of the deformation gradient $\boldsymbol{F}^{v}$ must be defined by a consistent flow rule obeying the remaining term $\frac{\partial\Omega}{\partial\boldsymbol{F}_{v}} : \dot{\boldsymbol{F}}_{v} \leqslant 0$ from the second law of thermodynamics. This is automatically satisfied by relating the viscous deformation rate tensor $\boldsymbol{D}^{v}$ to the viscous stress as (Garcia-Gonzalez, 2019):

$$\boldsymbol{D}^{v} = \boldsymbol{F}^{e}\dot{\boldsymbol{F}}^{v}\boldsymbol{F}^{-v}\boldsymbol{F}^{-e} = \frac{\boldsymbol{\sigma}^{v}_{\mathrm{m}}}{\sqrt{2}\eta} \tag{33}$$

with η being the polymer viscosity and $\boldsymbol{\sigma}^{v}_{\mathrm{m}}$ being the viscous contribution to the Cauchy stress tensor $\boldsymbol{\sigma}^{v}_{\mathrm{m}} = \boldsymbol{P}^{v}_{\mathrm{m}}\boldsymbol{F}^{T}$. The model formulation using the 8-chain approach for the mechanical response in one-dimensional case is presented in the *Appendix* with a set of scalar equations for the calibration with various sets of experimental data.

4. Model validation

This section aims at validating the physical assumptions made at the microscale and to see how they translate into the magneto-mechanical responses of MAPs at the macroscale. To this end, we first evaluate the model to predict experimental results for uniaxial loading conditions (mechanical and magnetic loading). Then, the model is tested at completely different loading conditions to further validate its microstructural nature. In this regard, model predictions are closely discussed by means of uniaxial tension and shear mechanical loadings at different strain rates with and without external magnetic fields. Note that all the magnetic parameters will be identified directly from their physical meaning and experimental data. Moreover, the mechanical parameters will be calibrated following the same optimisation procedure used in Refs.: Garcia-Gonzalez et al. (2018) and Garzon-Hernandez et al. (2020). In addition, note that the modelling framework presented at this stage does not include spatial discretisation and focuses mainly on the constitutive and microstructural features. This may represent a limitation as geometrical effects, i.e., magnetic fringing effects, are not accounted for in these simulations. Future work will implement the proposed constitutive equations in finite element frameworks to provide spatial discretisation and allow for incorporating such effects.

4.1. Magneto-mechanical uniaxial loading

Different sets of experimental data published in the literature are taken to validate the applicability of the proposed model. At first, we take the experimental data published by Schubert and Harrison (2015) for MAPs composed of silicone polymeric matrix filled with carbonyl iron powder (CIP) particles. Therein, they performed uniaxial tests at relatively large strains under quasi-static conditions for different concentrations of CIP ranging from $\phi = 0.0$ to $\phi = 0.3$. Moreover, these tests were conducted for pure a mechanical loading as well as under a magneto-mechanically coupled loading condition. For comparison with the proposed model, we take the experimental data performed on isotropic MAPs. Therefore, the representative lattice to compute the summation terms in Eqs. (25) and (30) is the one represented in Fig. 3a (isotropic distribution). In addition, the experimental data provided in Soria-Hernandez et al. (2019) are also used. They performed magneto-mechanical tests on a PDMS-CIP composite under a uniaxial tensile loading condition. The experimental data are related to MAPs with a preferred orientation (anisotropic) of the magnetic particles at different volume ratios (see Fig. 3b for particles distribution as perfectly aligned chains).

At first, the mechanical material parameters are identified using the two sets of experimental data mentioned above. The calibration is carried out for both experimental data and for both LP (Eq. 29_1) and 8-chain (Eq. 28_1) models, see *Mechanical, elastic* parameters in Tables 1 and 2. Fig. 3a shows the comparison between model predictions and the experimental data for MAPs with isotropic distribution of particles (Schubert and Harrison, 2015). The LP model is able to capture the nonlinear shape of the stress–strain curve, while the 8-chain model presents some limitations at the small stretch range. This is because of inherit incapability of the 8-chain model in capturing experimental data at very small strains (up to 20–30%), see Lopez-Pamies (2010). However, both approaches capture the stiffening effect observed when increasing the particles' volume ratios ϕ. Moreover, Fig. 3b presents the comparison between model predictions and the experimental data from Soria-Hernandez et al. (2019) of a MAP with chain-like distribution of particles. In this case, both LP and 8-

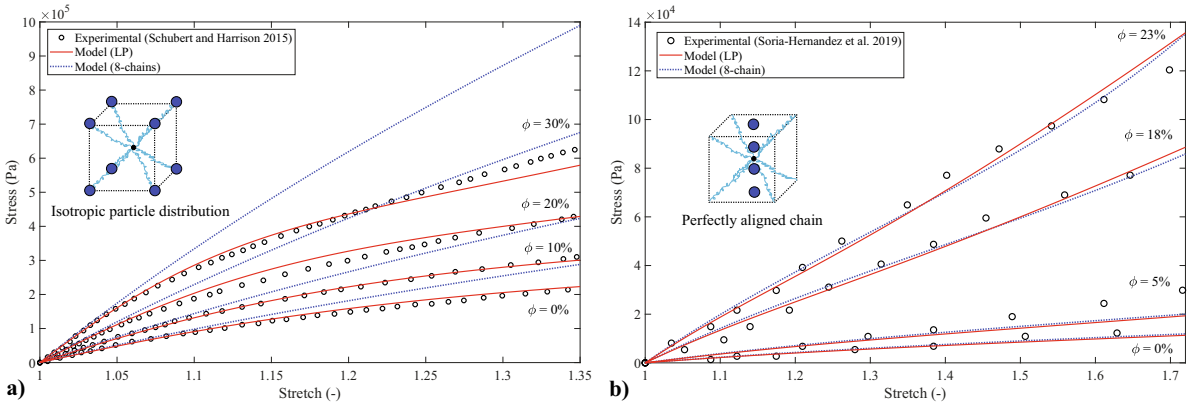

Fig. 3. a) A comparison between experimental data from Schubert and Harrison (2015) and model predictions for uniaxial tensile tests at different magnetic particle's volume ratio. A scheme of the representative lattice for isotropic MAPs is presented. Model parameters used are shown in Table 1. b) Comparison between experimental data (Soria-Hernandez et al., 2019) and model predictions for uniaxial tensile tests at different magnetic particle's volume ratio. A scheme of the representative lattice for chain-like MAPs is presented. Model parameters used are shown in Table 2.

Table 1
Constitutive parameters used in the simulations of Figs. 3a, 4, 6, 7a, 9, 10 and 11. Note that viscous properties are only provided for the LP model.

Mechanical parameters for 8-chain model							
G^e (kPa)	N_e $(-)$	G^v (kPa)	N_v $(-)$	η (Pas)	g $(-)$		
340	25	–	–	–	4.5		
Mechanical parameters for LP model							
G_1^e (kPa)	α_1^e $(-)$	G_2^e (kPa)	α_2^e $(-)$	G^v (kPa)	α^v $(-)$	η (Pas)	g $(-)$
200	1	140	-5	200	1	2000	4.5
Magnetic parameters							
M_s (kA/m)	μ_r $(-)$	μ_o (H/m)					
1582	21.5	$4\pi 10^{-7}$					

Table 2
Constitutive parameters used in the simulations of Figs. 3b, 6, 7b and 9. Note that viscous properties are only provided for the 8-chain model.

Mechanical parameters for 8-chain model							
G^e (kPa)	N_e $(-)$	G^v (kPa)	N_v $(-)$	η (Pas)	g $(-)$		
8	12	8	5	2000	10		
Mechanical parameters for LP model							
G_1^e (kPa)	α_1^e $(-)$	G_2^e (kPa)	α_2^e $(-)$	G^v (kPa)	α^v $(-)$	η (Pas)	g $(-)$
7	1.3	1	-1.2	–	–	–	10
Magnetic parameters							
M_s (kA/m)	μ_r $(-)$	μ_o (H/m)					
1582	21.5	$4\pi 10^{-7}$					

chain models suitably fit the non-linear response of the material as well as the stiffening effects for different ϕ.

Once mechanical parameters are identified, the magnetic parameters (M_s, μ_p, μ_o) associated with the CIP particles are taken from literature, see Arias et al. (2006) and in Tables 1 and 2. The effects of an external magnetic field on the tensile stress are presented in Fig. 4a. Here, we examine predictive capabilities of the proposed model by simulating the experimental data from Schubert and Harrison (2015). They conducted experiments on isotropic MAPs with different volume fractions of particles under the action of a constant magnetic field of 283 mT (milliTesla). Note that the LP model is used here for the mechanical part as it has a better capability in capturing mechanical stress–strain responses. Simulation results are presented in Fig. 4a, where it is vivid that if free mechanical boundary conditions are considered, a MAP would contract. In order to balance the compressive stress originated due to the magnetic field, a tensile force needs to be applied at the beginning to keep a MAP sample at $\lambda = 1$. Therefore, in Fig. 4, there is an initial stress at $\lambda = 1$.

When comparing these results with experimental observations from Schubert and Harrison (2015), a good predictive capability of the model can be inferred from different perspectives. Regarding the influences for the magnetic particles' content, a clear relationship can be observed: the higher the magnetic particles' volume ratio, the more relevant contributions to the magnetic stress. In addition, the model predicts an accurate quantitative estimation of stress values (note that no calibration is done at this stage). The discrepancy in stress at unit stretch may be explained by an experimental force balance or the adaptation of the experimental grips before performing the test to avoid any pre-stress due to the application of the magnetic field. Another potential explanation is the smooth application of the external magnetic field during the first stretching stage. In this regard, if the specimen is mechanically constraint, a magnetic field actuating on the MAP will introduce an internal stress due to magnetic particles interaction. Under free mechanical boundary conditions, the MAP will try to compress or expand (depending on the arrangement of the particles inside it). However, if neither a compression nor an expansion is allowed,

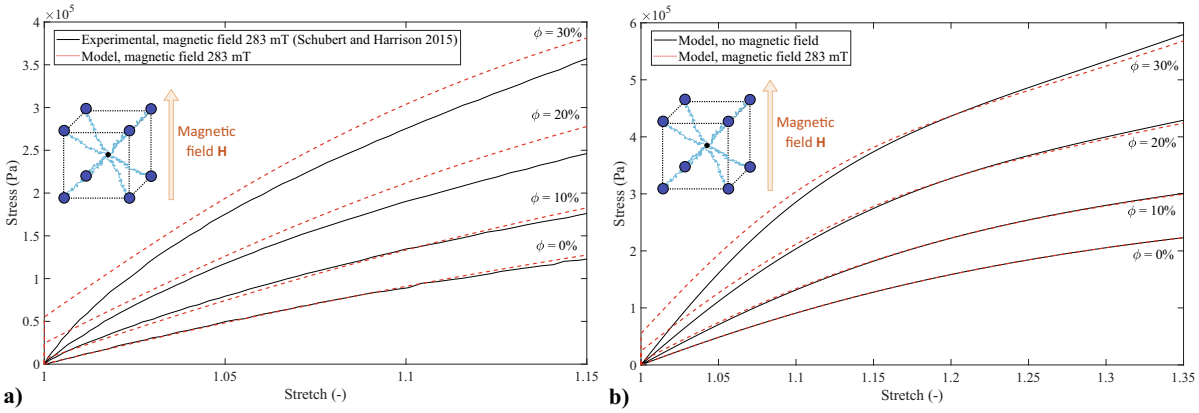

Fig. 4. a) A comparison between experimental data (Schubert and Harrison, 2015) and model predictions for uniaxial tensile tests at different magnetic particle's volume ratios. b) A comparison between model predictions for uniaxial tensile tests at different magnetic particle's volume ratios under the action of an external magnetic field and under a null magnetic field. Model parameters used are shown in Table 1.

an internal stress will appear as predicted by the proposed model. Moreover, we provide a comparison between model predictions for tensile loading under the action of an external magnetic field and under null magnetic field, see Fig. 4b. The model predictions capture the relative influence of the magnetic stress during the stretching process. In this regard, an important magnetic stress contribution is observed at the beginning of the tests leading to higher stresses when the magnetic field is active for all the particle's contents. However, this difference in stress with respect to the corresponding test without external magnetic field decreases with stretch leading to the eventual crossing between curves. These results are also consistent with experimental observations by Schubert and Harrison (2015).

Additionally, we simulate magneto-mechanical responses for perfectly aligned chain-like anisotropic MAPs. In this regard, Fig. 5 shows the model predictions for quasi-static tensile behaviour with different magnetic particles' volume ratios, where the MAP is subjected to an increasing magnetic field up to 200 kA/m along the loading direction. Note that, unlike Fig. 4 where a constant magnetic field is applied, a constant magnetic field rate is applied in Fig. 5. These predictions are compared with simulations at null magnetic field conditions and computed using the 8-chain model for the mechanical part. When comparing these results with the observations from Soria-Hernandez et al. (2019), a good correlation is found. For instance, the magnetic contribution to the stress is more significant with the increase of particles' volume fractions. Moreover, the influence increases with the application of the magnetic field up to a given stretch value ($\lambda = 1.2$) and, from this point, it progressively reduces leading to the convergence of the stress–strain curves with and without magnetic field applied. Note that, in this case with a perfectly aligned chain-like distribution of magnetic particles is assumed. Hence, the stress component along the magnetic/stretching direction is always equal to or higher than the corresponding one without the application of a magnetic field.

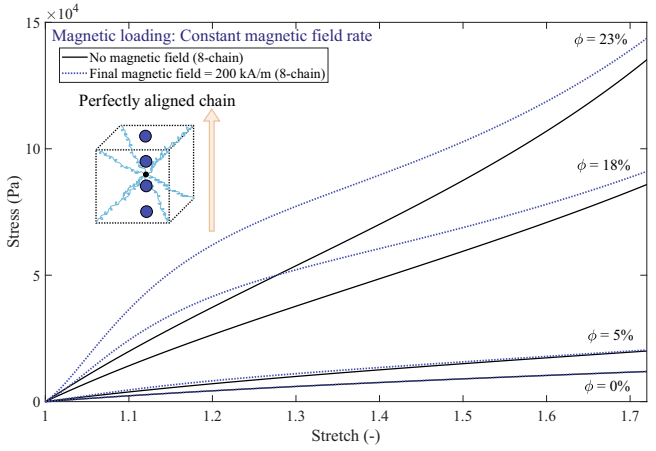

Fig. 5. Comparison between model predictions for uniaxial tensile tests at different magnetic particle's volume ratio and different magnetic conditions, with and without external magnetic field for: a) isotropic distribution of magnetic particles. Model parameters used are shown in Table 1.; b) chain-like distribution of magnetic particles. Model parameters used are shown in Table 2.

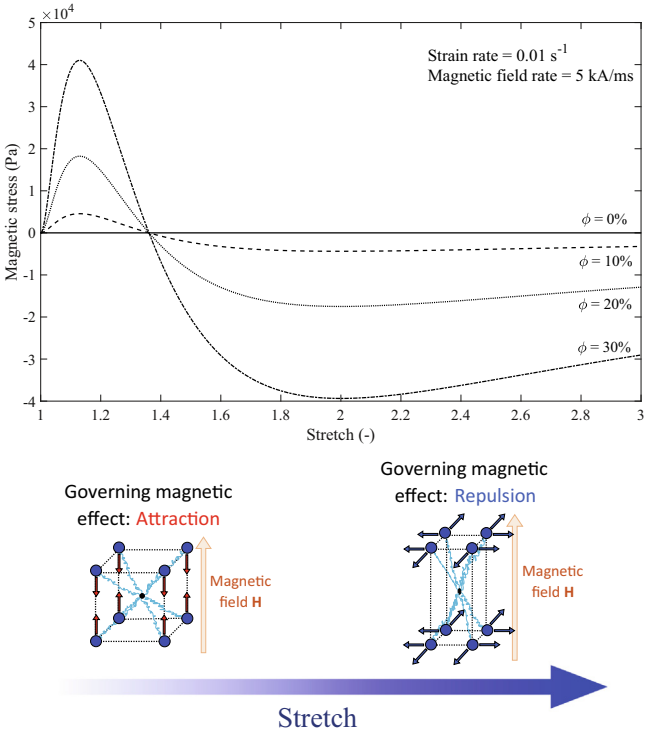

Fig. 6. Magnetic stress evolution with the application of a constant magnetic field rate and a constant strain rate (Eq. (30)) for different magnetic particle's volume ratios. The stress presented corresponds to the stress component along the loading direction. Magnetic model parameters used are shown in Tables 1 and 2.

To analyse further, we simulate different scenarios isolating the magnetic contribution from the total stress in Fig. 6. In this regard, a constant magnetic field rate along with a constant strain rate (both along the same material direction) is applied. A continuous increase of the magnetic stress in the loading direction is observed until a stretch of around 1.18. The stress contribution is mainly governed by attraction forces between particles along the field direction (see Fig. 6). At some point, the magnetic particles reach the saturation magnetisation M_s. From this point, the stretch increase leads to larger distances between magnetic particles along the direction of the field, resulting in a significant reduction of the dipole–dipole interactions. This tendency continues until the particles are too far that no significant magnetic stress contribution is observed along the loading direction. However, the particles along the perpendicular directions to the field come closer due to the Poisson's effect. The approaching particles perpendicular to the loading direction results in stress contributions that are mainly governed by repulsion forces (see Fig. 6). Thus, the resultant magnetic stress along the stretching direction (same as the field direction) inverses its sign. From this point, larger stretches contribute to the rearrangement of the particles leading to a chain-like particles' distribution perpendicular to the field direction. This new arrangement of the particles finally leads to the reduction of magnetic stress. Note that the analysis presented here is carried out for isotropic distribution of the magnetic particles. Further microstructural analyses will be presented in Section 5.

Finally, a generic viscosity of η = 2000 Pas is selected to evaluate the capability of both LP and 8-chain models to capture strain rate dependences. Model simulations for different magnetic particle's volume fractions and two different strain rates are shown in Fig. 7. A stiffer response is observed at higher strain rates and its relative importance is shown to decrease with the magnetic particle's volume ratio which are common characteristics of polymeric materials.

4.2. Magneto-mechanical shear loading

In the previous section, the physical consistency of the proposed microstructural-based model is verified under uniaxial tensile loading. Here, the model is validated for a different loading scenario, i.e., shear data at different strain rates and magnetic conditions. To this end, the work published by Pelteret et al. (2018) is taken as a reference. In the study, they considered a parallel-plate rotational rheometer which introduces a shear-like deformation within a MAP that, at the same time, is subjected to an external magnetic field in the axial direction. These tests are performed at different strain rates showing a significant influence on material stiffness and hysteresis loops (see Fig. 8).

At first, the material parameters are calibrated to provide the same stress levels as in Pelteret et al. (2018) (Fig. 8a). The calibrated parameters are presented in Table 3 for the 8-chain approach. Then, the identified parameters are used to validate the model for the material at higher deformation rates (Fig. 8b). Note that our simulations start from a completely relaxed state (deformation gradient equal to second order unit tensor) where we only use one linear term for the viscous contribution (Eq. (33)). The results presented in Fig. 8 show the ability of the model to reproduce a shear loading on MAPs. In this regard, stiffer responses are obtained when applying an external magnetic field, independently of the strain rate or the shear direction. Moreover, the viscous contributions are evident in both the nonlinear hysteresis loops and strain rate dependency by means of a material stiffness. Therefore, this analysis provides a good validation of the model hypothesis to predict the response of MAPs under a mechanical shear load and a magnetic load at different strain rates accounting for viscous deformation mechanisms.

5. Microstructural influences predicted by the model

A salient feature of the proposed microstructural-based magneto-mechanically coupled model is that it allows for predicting the mechanical responses to magnetic fields depending on the arrangement of the particles within a polymeric matrix. This section considers various options of the magnetic particles distributions within a MAP and evaluates their influences on the magneto-mechanical stress contributions (see Fig. 1 for different particle distributions). To this end, we apply a constant strain rate and a constant magnetic field rate along the same material direction (same loading conditions as in Fig. 6). Simulations are conducted taking three forms of particle distributions, i.e., isotropic distribution; perfectly aligned chains along the stretch and field direction; and perfectly aligned chains perpendicular to the stretch and field direction. Results are shown in Fig. 9 along with representative schemes of the particle distributions considered. The evolution of the magnetic stress with stretch and magnetic field for the isotropic distribution was previously discussed in detail in Section 4.1. We may recall the change in the sign of the stress contribution with the evolution of the stretch as a result of the attenuation of attraction forces along the stretch/field direction. On the contrary, the intensification of repulsion forces perpendicular to the stretch/field direction (see scheme in Fig. 6) is revisited. Moreover, when the magnetic particles are distributed forming perfectly aligned chains, these effects are not presented and only

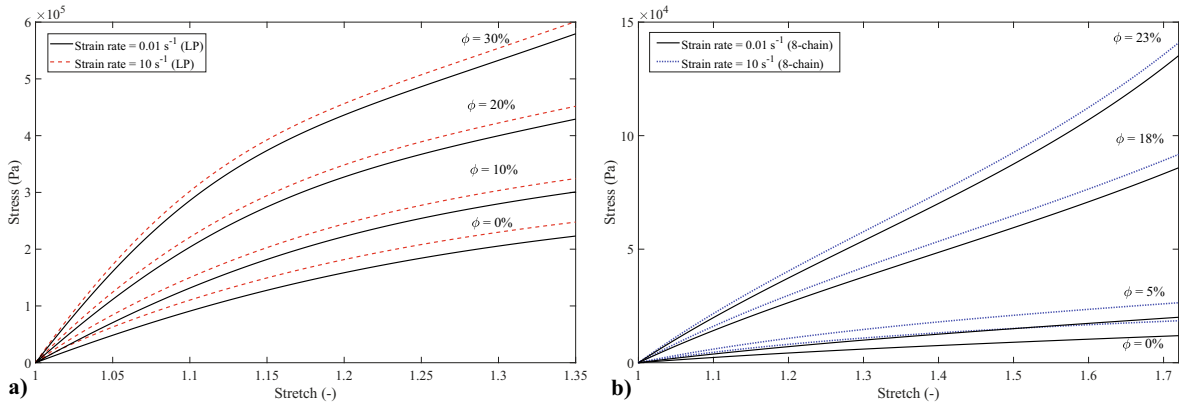

Fig. 7. Total stress dependence on strain rate for different magnetic particle's volume ratios. The stress presented corresponds to the stress component along the loading direction using: a) the LP model with parameters provided in Table 1; a) the 8-chain model with parameters provided in Table 2.

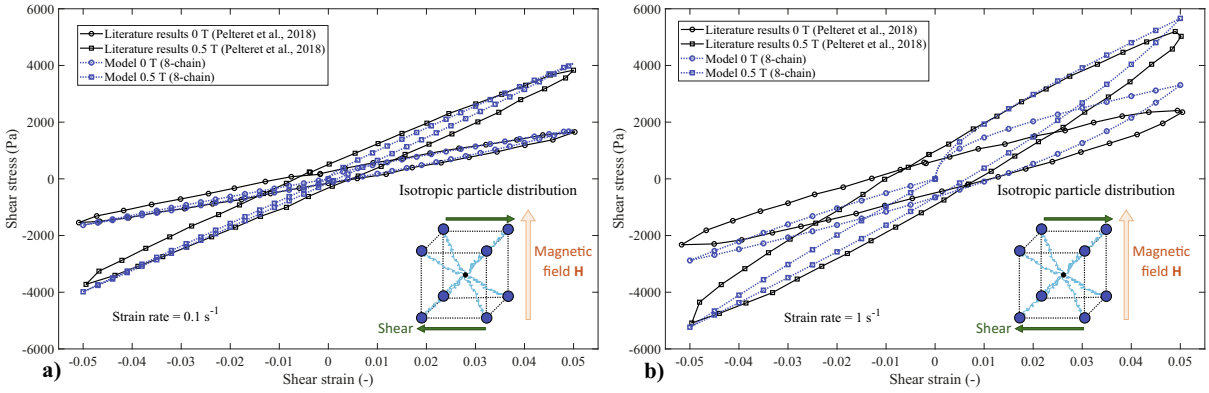

Fig. 8. Comparisons between literature data (Pelteret et al., 2018) and model predictions for shear tests with and without the application of an external magnetic field at different strain rates: a) $0.1s^{-1}$; b) $1s^{-1}$. Model parameters used are shown in Table 3 along with $\phi = 0.075$.

Table 3
Constitutive parameters used in the simulations of Fig. 8.

Mechanical parameters for 8-chain model					
G^e (kPa)	N_e $(-)$	G^v (kPa)	N_v $(-)$	η (Pas)	g $(-)$
25	25	800	5	2000	–
Magnetic parameters					
M_s (kA/m)	μ_r $(-)$	μ_o (H/m)			
1582	21.5	$4\pi 10^{-7}$			

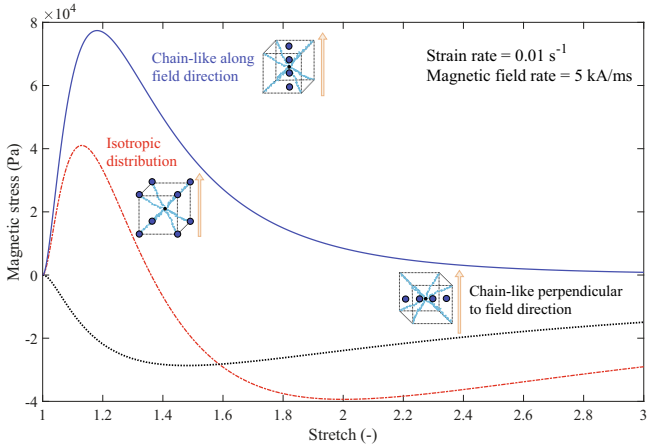

Fig. 9. Magnetic stress evolution with the application of a constant magnetic field rate and a constant strain rate (Eq. (30)) for different magnetic particle's distributions: isotropic distribution (red); chain-like along magnetic field direction (blue); chain-like perpendicular to magnetic field direction (black). The stress presented corresponds to the stress component along the loading direction. Magnetic model parameters used are shown in Tables 1 and 2. (For interpretation of the references to color in this figure legend, the reader is referred to the web version of this article.)

attraction forces or repulsion forces for the case of chains along the field or perpendicular to the field, respectively, govern MAP responses. In contrast to the isotropic case (dash line), in a chain-like anisotropic structure, a higher influence of the magnetic contribution is observed (solid line). This last observation is also consistent with the experimental results presented in Schubert and Harrison (2015). For the chain-like anisotropic case, an increase in magnetic stress is observed with the application of the magnetic field until it reaches the magnetisation saturation value. From this point, as the stretch is still increased, the particles are far from each other resulting in lower magnetic interactions. This tendency continues until the particles are too far that no significant stress contribution is observed. A similar tendency is observed for chains aligned perpendicular to the field but with opposite sign in the stress contribution, consistent with the observations from the analysis conducted in Fig. 6. It is worth to mention that the results provided by the proposed finite strain continuum framework are consistent with computational approaches that explicitly consider polymeric matrix and magnetic particles as two different phases (see, for example, microstructural simulations performed in Keip and Sridhar (2019), Mukherjee et al. (2020) and Zabihyan et al. (2020).

Note that all the previous analysis presented considered distributions of the magnetic particles either as perfectly isotropic or perfectly aligned chains. From an experimental point of view, most manufacturing processes of MAPs usually impose a magnetic field during curing to induce a preferred orientation of the particles leading to chain like distributions, see, for instance, Fig. 1 in Hossain et al. (2015a). However, this alignment of particles forming the chains is not perfect and presents a certain grade of waviness (see wavy distributions in Fig. 1). Therefore, a more realistic arrangement of the magnetic particles is considered here. In this regard, we assume that MAP specimens formed by a polymeric matrix filled with particles oriented along a preferred direction (X axis in Fig. 10). Therefore, the distribution of the particles inside the MAP can be assumed as chains sufficiently far from each other that are not interacting between them. For that, we determine the distribution of the particles forming the chain as dependent on two parameters (see Fig. 10): a distance between particles along the chain direction δ_x; and a distance between particles along the perpendicular direction to the chain orientation δ_y. Thus, the factor δ_y/δ_x determines how "wavy" the particles chain is while $\delta_y/\delta_x = 0$ leads to perfectly aligned chains, and higher values of this wavy factor indicates worse alignment of particles. Note that high enough values of δ_y/δ_x results, in practical terms, into two individual perfectly aligned chains with distance between particles equal to $2\delta_x$. To analyse the effect of particles' alignment along the chains, we performed simulations of the response of a MAP with different wavy factors δ_y/δ_x ranging from 0 to 2. In these cases, a

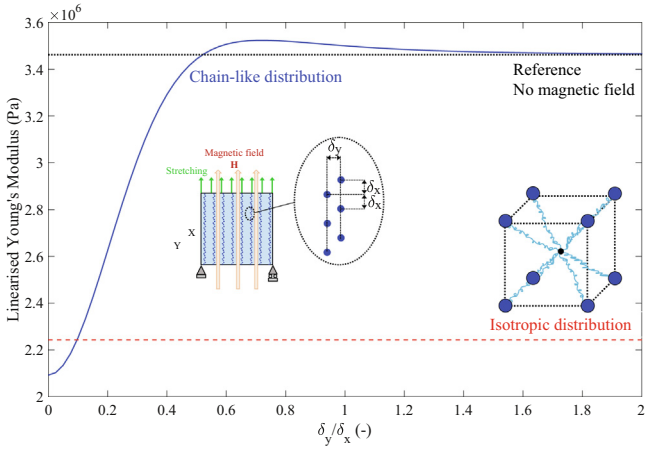

Fig. 10. Dependence of the linearised Young's modulus on the MAP's microstructure under the influence of a constant magnetic field of 100 kA/m. This figure compares a reference modulus when a null magnetic field is applied with: isotropic distribution of magnetic particles (red); wavy chain distribution of the particles accounting for different values of the wavy factor δ_y/δ_x (blue). Model parameters used are shown in Table 1 (LP model). (For interpretation of the references to color in this figure legend, the reader is referred to the web version of this article.)

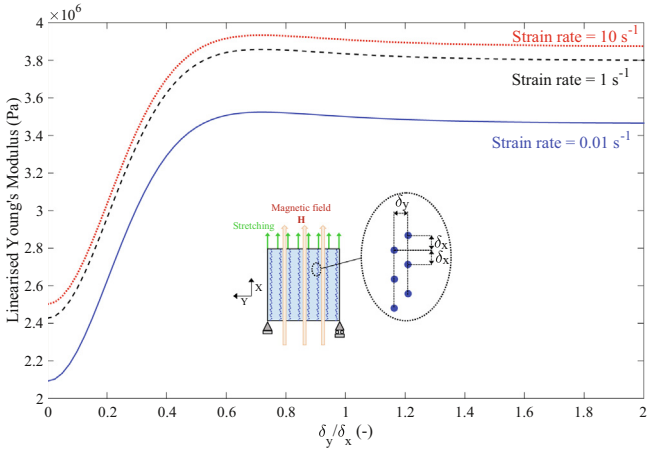

Fig. 11. Dependence of the linearised Young's modulus on the MAP's microstructure and strain rate under the influence of a constant magnetic field of 100 kA/m. This figure compares the response of a wavy chain distribution of the particles accounting for different values of the wavy factor δ_y/δ_x at different rates. Model parameters used are shown in Table 1 (LP model).

cube specimen with all the particles' chains aligned along the X direction is defined. One of the cube's sides perpendicular to the chains orientation is restricted to not move in this direction X. A constant strain rate along X direction (low enough to assume quasi-static conditions) is applied on the opposite side of the cube. In addition, a constant magnetic field is applied in the same direction (X). A scheme of the boundary and loading conditions applied is shown in Fig. 10 (wavy chain distribution picture).

The effects of a magnetic field on different stiffness moduli (e.g., shear and elastic moduli) is a critical issue that has been microstructurally investigated by many theoretical works, see Han et al. (2013) and Ivaneyko et al. (2011). Note that the stiffness moduli under a magnetic load largely depend on particles arrangements. Therefore, it is crucial to analyse the influences of the wavy factor δ_y/δ_x on the stiffness moduli, e.g., on an effective linearised Young's modulus. The effective linearised Young's modulus is understood here as the initial stiffness of the global MAP response (considering both mechanical and magnetic contributions to the stress). The modulus for a MAP under a null magnetic field is shown in Fig. 10 as the reference, as well as the corresponding linearised Young's modulus for an isotropic distribution of the particles. We can observe a completely different mechanical response of the MAP under the application of a magnetic field depending on the arrangement of the particles. In this regard, when the particles are perfectly aligned along the X direction, i.e., $\delta_y/\delta_x = 0$, the magnetic field applied in X presents the highest influence into the effective stiffness. Note that in this study, a magnetic field reduces the stiffness maximally for the case of chain-like anisotropic MAPs which is consistent with many theoretical studies (Borcea and Bruno, 2001; Kankanala and Triantafyllidis, 2004; Han et al., 2013; Ivaneyko et al., 2011). However, the effect is continuously decreased with the increase of the wavy factor, even leading to reverse effects at a given critical value (here identified at $\delta_y/\delta_x \approx 0.55$). Before the critical value, a tensile internal stress arises from attraction magnetic forces along X direction, indicating that the MAP tries to contract along the applied magnetic field direction. Note that the model parameters presented in Table 1 with $\phi = 0.3$ have been used for these simulations, so the stress-stretch curves of the material are the corresponding ones from Fig. 3a. Due to the incompressibility condition assumed on the MAP, the magnetic field also introduces a strong volumetric component that governs the material response over the mechanical stress leading to a decrease in the stiffness. However, for wavy factors larger than the critical one, the distribution of the magnetic particles favours the repulsion forces between particles (see scheme in Fig. 6) leading to an internal elongation of the MAP along the field direction, in turn resulting into an increase of the stiffness. Moreover, large enough values of the wavy factor result into "isolation" of the magnetic particles considerably reducing the effect of the magnetic field on the mechanical response. In addition, we evaluate the effect of strain rate on these magnetic effects. To this end, the linearised Young's modulus of the MAP depending on the way factor is plotted for different strain rate conditions in Fig. 11. We can observe the same tendencies as for quasi-static conditions but with an offset in the linearised Young's modulus due to the strain rate hardening effects.

Overall, the results presented in this section illustrate the flexibility of the proposed model to account for microstructural features of MAPs and to predict their overall macroscopic properties. To this end, the microstructural arrangements of the magnetic particles within the MAP is described on the basis of a characteristic lattice. This characteristic lattice is scaled up to provide the macroscopic magneto-mechanical response of the MAP by adopting an affine network homogenisation. This framework provides thus a microstructural-based constitutive alternative to other relevant approaches such as: variationally consistent phase-field approach (Keip and Sridhar, 2019); microstructurally-guided explicit continuum models (Mukherjee et al., 2020); FE^2 approaches (Zabihyan et al., 2020).

6. Conclusions

Most of the current approaches to model the magneto-mechanical behaviour of magneto-active polymers (MAPs) are based on phenomenological continuum models. These models are relative good in capturing the main features of MAPs' response to external mechanical and/or magnetic stimuli. However, they still present limitations to understand some of the underlying physics such as the effects of magnetic particles' arrangement within the polymeric matrix and their interactions with the external magnetic field. Novel approaches in the literature, such as the relevant works in Keip and Sridhar (2019), Mukherjee et al. (2020) and Zabihyan et al. (2020), provide links between microstructural features and

the final continuum formulations. An alternative to these approaches is to formulate the constitutive equations from a characteristic lattice (Ivaneyko et al., 2012, 2014; Han et al., 2013). However, the current version of the lattice model is still limited to infinitesimal deformation theories and does not incorporate viscoelastic behaviours of MAPs. To the best of the authors' knowledge, this work, for the first time, proposes a continuum model with direct links to the MAP microstructure accounting for viscous (rate) dependences, non-linear mechanical response and magneto-mechanical coupling within a thermodynamically consistent framework. The proposed model is calibrated with experimental data from the literature and its fundamentals are validated with further published experimental evidences. Once validated, the microstructural flexibility of the model is extensively explained and we provide potential explanation to different observations in MAPs such as the stiffening or softening and the expansion or compression of MAPs under magnetic stimuli. In this regard, we point to the distribution of magnetic particles forming irregular wavy chains as a potential factor determining the consequences of magnetic fields on the mechanical responses of MAPs. Future avenues may address the implementation of this model into FE solvers to explore heterogeneous distribution of the magnetic particles (i.e., isotropic, wavy chains with different preferred orientation) leading to "programmed" instabilities (see Goshkoderia et al. (2020) for stability related analysis). Other future efforts may focus on extensions of the proposed constitutive framework to model magneto-active hydrogels or to incorporate dependences related to the magnetic particles' shape (Goshkoderia and Rudykh, 2017).

Declaration of Competing Interest

The authors declare that they have no known competing financial interests or personal relationships that could have appeared to influence the work reported in this paper.

Acknowledgement

The authors acknowledge the financial support of the mobility internship for researchers of Carlos III University of Madrid (Spain) ("Programa propio de investigacion - Convocatoria 2020 movilidada") that facilitates a research visit of the first author to Zienkiewicz Centre for Computational Engineering (ZCCE) at Swansea University, UK. DGG acknowledges support from Programa de Apoyo a la Realizacion de Proyectos Interdiscisplinares de I+D para Jovenes Investigadores de la Universidad Carlos III de Madrid and Comunidad de Madrid (project: BIOMASKIN), support from the Talent Attraction grant (CM 2018-2018-T2/IND-9992) from the Comunidad de Madrid, and support from the European Research Council (ERC) under the European Union's Horizon 2020 research and innovation programme (grant agreement No. 947723). MH acknowledges the funding through an EPSRC Impact Acceleration Award (2020-2021).

Appendix A. 1D formulation of the model

This appendix simplifies the model for one-dimensional (1D) simulations where both the stretching and magnetic field are applied along the same direction (hereafter referred to as X). The sets of 1D equations to address uniaxial magneto-mechanical loading, as well as their explicit implementation, are provided for a quick testing of the 8-chain model and faster calibration purposes. To this end, a scalar function of the XX component of $\boldsymbol{P}$, P_{XX}, according to Eq. (15) is derived depending on the stretch along X direction λ, the XX and YY components of the viscous deformation gradient F^v_{XX} and F^v_{YY}, and the X component of the magnetic field H_X as:

$$P_{XX}\left(\lambda, F^v_{XX}, F^v_{YY}, H_X\right) = P^e_{m,XX}(\lambda) + P^v_{m,XX}\left(\lambda, F^v_{XX}, F^v_{YY}\right) + P_{mg,XX}(\lambda, H_X) - p\left(\lambda, F^v_{XX}, F^v_{YY}, H_X\right)/\lambda \tag{A.1}$$

Note that isotropic conditions are assumed leading to $F^v_{ZZ} = F^v_{YY}$, as well as incompressible conditions leading to the following form of the deformation gradient:

$$\boldsymbol{F} = \begin{bmatrix} \lambda & 0 & 0 \\ 0 & 1/\sqrt{\lambda} & 0 \\ 0 & 0 & 1/\sqrt{\lambda} \end{bmatrix} \tag{A.2}$$

The elastic component of the 1D mechanical stress can be written as:

$$P^e_{m,XX} = [1-\phi]\left[2XG^e\sum_{k=1}^{K}\frac{kC_k}{N_e^{k-1}}I_{1,h}^{k-1}\right]\lambda \tag{A.3}$$

where the term $I_{1,h}$ reads as:

$$I_{1,h} = X\left[\lambda^2 + \frac{2}{\lambda} - 3\right] + 3 \tag{A.4}$$

Moreover, the viscous component of the 1D mechanical stress can be written as:

$$P^v_{m,XX} = [1-\phi]\left[2G^v\sum_{k=1}^{K}\frac{kC_k}{N_v^{k-1}}\left(I_1^e\right)^{k-1}\right]\frac{\lambda}{\left[F^v_{XX}\right]^2} \tag{A.5}$$

where the term I_1^e reads as:

$$I_1^e = \frac{\lambda^2}{\left[F^v_{XX}\right]^2} + \frac{2}{\lambda\left[F^v_{YY}\right]^2} \tag{A.6}$$

Regarding the 1D magnetic stress, it can be computed as:

$$P_{mg,XX} = -\frac{\mu_r\mu_o}{4\pi} \times \frac{\phi^2 M_X^2}{\gamma}\sum_i\left[-\frac{15\left[R^0_{i,X}\right]^4\lambda}{\|\boldsymbol{FR}_i^0\|^7} + \frac{2}{\lambda^3\|\boldsymbol{FR}_i^0\|^3} - \frac{3\left[R^0_{i,X}\right]^2}{\lambda\|\boldsymbol{FR}_i^0\|^5}\right] \tag{A.7}$$

with:

$$\boldsymbol{FR}_i^0 = \begin{pmatrix} \lambda R^0_{i,X} \\ R^0_{i,Y}/\sqrt{\lambda} \\ R^0_{i,Z}/\sqrt{\lambda} \end{pmatrix} \tag{A.8}$$

and, therefore:

$$\|\boldsymbol{FR}_i^0\| = \left[\lambda^2\left[R^0_{i,X}\right]^2 + \frac{\left[R^0_{i,Y}\right]^2}{\lambda} + \frac{\left[R^0_{i,Z}\right]^2}{\lambda}\right]^{1/2} \tag{A.9}$$

The pressure term p is defined from boundary conditions. For uniaxial loading and isotropic MAPs it becomes:

$$p = \left(P^e_{m,YY} + P^v_{m,YY} + P_{mg,YY}\right)/\sqrt{\lambda} = \left(P^e_{m,ZZ} + P^v_{m,ZZ} + P_{mg,ZZ}\right)/\sqrt{\lambda} \tag{A.10}$$

where:

$$P^e_{m,YY} = P^e_{m,ZZ} = [1-\phi]\left[2XG^e\sum_{k=1}^{K}\frac{kC_k}{N_e^{k-1}}I_{1,h}^{k-1}\right]\frac{1}{\sqrt{\lambda}} \tag{A.11}$$

$$P^v_{m,YY} = P^v_{m,ZZ} = [1-\phi]\left[2G^v\sum_{k=1}^{K}\frac{kC_k}{N_v^{k-1}}\left(I_1^e\right)^{k-1}\right]\frac{1}{\sqrt{\lambda}\left[F^v_{YY}\right]^2} \tag{A.12}$$

$$P_{mg,YY} = P_{mg,ZZ} = -\frac{\mu_r \mu_o}{4\pi}\frac{\phi^2 M_X^2}{\gamma}\sum_i\left[-\frac{15\left[R^0_{i,X}\right]^2\left[R^0_{i,Y}\right]^2}{\sqrt{\lambda}\|\boldsymbol{FR}^0_i\|^7} - \frac{3\left[R^0_{i,Y}\right]^2}{\lambda^{5/2}\|\boldsymbol{FR}^0_i\|^5}\right] \tag{A.13}$$

The magnetisation M_X can be written as a function of the X component of the magnetic field H_X as:

$$M_X = \frac{M_s[\mu_r - 1]H_X}{M_s + [\mu_r - 1]H_X} \tag{A.14}$$

Finally, the evolution of F^v_{XX} and F^v_{YY} can be explicitly integrated, using the flow rule given by Eqn. (33), as:

$$F^{v,n+1}_{XX} = F^{v,n}_{XX} + \frac{\Delta t}{\sqrt{2}\eta}F^{v,n}_{XX}\sigma^v_{\mathrm{m},XX} \tag{A.15}$$

$$F^{v,n+1}_{YY} = F^{v,n+1}_{ZZ} = F^{v,n}_{YY} + \frac{\Delta t}{\sqrt{2}\eta}F^{v,n}_{YY}\sigma^v_{\mathrm{m},YY} \tag{A.16}$$

where Δt is the time increment, $n+1$ and n refer to current and previous step values, and:

$$\sigma^v_{\mathrm{m},XX} = [1-\phi]\left[2XG^e\sum_{k=1}^{K}\frac{kC_k}{N_e^{k-1}}I_{1,h}^{k-1}\right]\frac{\lambda^2}{\left[F^v_{XX}\right]^2} \tag{A.17}$$

$$\sigma^v_{\mathrm{m},YY} = [1-\phi]\left[2XG^e\sum_{k=1}^{K}\frac{kC_k}{N_e^{k-1}}I_{1,h}^{k-1}\right]\frac{1}{\lambda\left[F^v_{YY}\right]^2} \tag{A.18}$$

References

Alshammari, B.A., Al-Mubaddel, F.S., Karim, M.R., Hossain, M., Al-Mutairi, A.S., Wilkinson, A.N., 2019. Addition of graphite filler to enhance electrical, morphological, thermal, and mechanical properties in 500 poly (ethylene terephthalate): Experimental characterization and material modeling. Polymers 11 (9), 1411.

Arias, J.L., Gallardo, V., Linares-Molinero, F., Delgado, A.V., 2006. Journal of Colloid and Interface Science 299, 599.

Arruda, E.M., Boyce, M.C., 1993. A three-dimensional constitutive model for the large stretch behavior of rubber elastic materials. Journal of Mechanics and Physics of Solids 41, 389–412.

Bastola, A.K., Hossain, M., 2020. A review on magneto-mechanical characterizations of magnetorheological elastomers. Composites Part B: Engineering, 108348.

Bednarek, S., 1999. The giant magnetostriction in ferromagnetic composites within an elastomer matrix. Applied Physics A 68, 63–67.

Bellan, C., Bossis, G., 2002. Field dependence of viscoelastic properties of MR elastomers. International Journal of Modern Physics B 16, 2447–2453.

Bica, I., 2012. The influence of the magnetic field on the elastic properties of anisotropic magnetorheological elastomers. Journal of Industrial and Engineering Chemistry 18, 1666–1669.

Boczkowska, A., Awietjan, S.F., 2009. Smart composites of urethane elastomers with carbonyl iron. Journal of Materials Science 44, 4104–4111.

Boczkowska, A., Awietjan, S.F., 2012. Microstructure and properties of magnetorheological elastomers. In: Boczkowska, A. (Ed.), Advanced Elastomers-Technology, Properties and Applications, pp. 147–180. doi: 10.5772/2784..

Borcea, L., Bruno, O., 2001. On the magneto-elastic properties of elastomer-ferromagnet composites. Journal of Mechanics and Physics of Solids 49, 2877.

Böse, H., 2007. Viscoelastic properties of silicone-based magnetorheological elastomers. International Journal of Modern Physics B 21, 4790–4797.

Bosnjak, N., Nadimpalli, S., Okumura, D., Chester, S.A., 2020. Experiments and modeling of the viscoelastic behavior of polymeric gels. Journal of the Mechanics and Physics of Solids 136, 103829.

Brigadnov, I.A., Dorfmann, A., 2003. Mathematical modeling of magneto-sensitive elastomers. International Journal of Solids Structures 40, 4659–4674.

Brown, W.F., 1966. Magnetoelastic Interactions. Springer, Berlin.

Bustamante, R., 2010. Transversely isotropic nonlinear magneto-active elastomers. Acta Mechanica 210 (3–4), 183–214.

Bustamante, R., Dorfmann, L., Ogden, R.W., 2008. On variational formulations in nonlinear magnetoelastostatics. Mathematics and Mechanics of Solids 13, 725–745.

Coleman, B.D., Gurtin, M.E., 1967. Thermodynamics with internal state variables. Journal of Chemical Physics 47, 597–613.

Coquelle, E., Bossis, G., 2005. Magnetostriction and piezoresistivity in elastomers filled with magnetic particles. Journal of Advanced Science 17, 132–133.

Davidson, J.D., Goulbourne, N.C., 2013. A nonaffine network model for elastomers undergoing finite deformations. Journal of the Mechanics and Physics of Solids 61, 1784–1797.

de Souza Neto, E.D., Peric, D., Owen, D.R.J., 2008. Computational Methods for Plasticity: Theory and Applications. Wiley.

Diguet, G., Beaugnon, E., Cavaille, J.Y., 2010. Shape effect in the magnetostriction of ferromagnetic composite. Journal of Magnetism and Magnetic Materials 322, 3337.

Dorfmann, A., Ogden, R.W., 2004a. Nonlinear magnetoelastic deformations of elastomers. Acta Mechanica 167 (1–2), 13–28.

Dorfmann, A., Ogden, R.W., 2004b. Nonlinear magnetoelastic deformations. Quarterly Journal of Mechanics and Applied Mathematics 57 (4), 599–622.

Eringen, A.C., Maugin, G.A., 1990. Electrodynamics of Continua. Springer-Verlag.

Gao, W., Wang, X., 2019. Experimental and theoretical investigations on magnetoelastic shear behavior of isotropic MR elastomers under gradient magnetic fields. Journal of Magnetism and Magnetic Materials 483, 196–204.

Garcia-Gonzalez, D., 2019. Magneto-visco-hyperelasticity for hard-magnetic soft materials: theory and numerical applications. Smart Materials and Structures 28, 085020.

Garcia-Gonzalez, D., Landis, C.M., 2020. Magneto-diffusion-viscohyperelasticity for magneto-active hydrogels: rate dependences across time scales. Journal of the Mechanics and Physics of Solids 139, 103934.

Garcia-Gonzalez, D., Jérusalem, A., Garzon-Hernandez, S., Zaera, R., Arias, A., 2018. A continuum mechanics constitutive framework for transverse isotropic soft tissues. Journal of the Mechanics and Physics of Solids 112, 209–224.

Garzon-Hernandez, S., Arias, A., Garcia-Gonzalez, D., 2020. A continuum constitutive model for FDM 3D printed thermoplastics. Composites Part B: Engineering, 108373.

Ginder, J.M., Nichols, M.E., Elie, L.D., Tardiff, J.L., 1999. Magnetorheological elastomers: properties and applications. In: Wuttig, M.R. (Ed.), SPIE Proceedings 3675, Smart Structures and Materials: Smart Materials Technologies. SPIE Press, pp. 131–138.

Ginder, J.M., Nichols, M.E., Elie, L.D., Clark, S.M., 2000. Controllable stiffness components based on magnetorheological elastomers. In: Wereley, N.M. (Ed.), Smart Structures and Materials: Smart Structures and Integrated Systems, SPIE Proceedings 3985, SPIE Press, pp. 418–425..

Ginder, J.M., Schlotter, W.F., Nichols, M.E., 2001. Magnetorheological elastomers in tunable vibration absorbers. In: Inman, D.J. (Ed.), Smart Structures and Materials: Damping and Isolation, SPIE Proceedings 4331, SPIE Press, pp. 103–110..

Gordaninejad, F., Wang, X., Mysore, P., 2012. Behavior of thick magnetorheological elastomers. Journal of Intelligent Material Systems and Structures 23 (9), 1033–1039.

Goshkoderia, A., Rudykh, S., 2017. Stability of magnetoactive composites with periodic microstructures undergoing finite strains in the presence of a magnetic field. Composites Part B: Engineering 128, 19–29.

Goshkoderia, A., Chen, V., Li, J., Juhl, A., Buskohl, P., Rudykh, S., 2020. Instability-Induced Pattern Formations in Soft Magnetoactive Composites. Physical Review Letters 124, (15) 158002.

Griffiths, D.J., 1998. Introduction to Electrodynamics. Prentice Hall.

Haldar, K., Kiefer, B., Menzel, A., 2016. Finite element simulation of rate-dependent magneto-active polymer response. Smart Materials and Structures 25, 104003.

Han, Y., Hong, W., Faidley, L.E., 2013. Field-stiffening effect of magneto-rheological elastomers. International Journal of Solids and Structures 50 (14), 2281–2288.

Hossain, M., Saxena, P., Steinmann, P., 2015a. Modelling the mechanical aspects of the curing process of magneto-sensitive elastomeric materials. International Journal of Solids and Structures 58, 257–269.

Hossain, M., Saxena, P., Steinmann, P., 2015b. Modelling the curing process in magneto-sensitive polymers: rate-dependence and shrinkage. International Journal of Non-Linear Mechanics 74, 108–121.

Hossain, M., Chatzigeorgiou, G., Meraghni, F., Steinmann, P., 2015c. A multi-scale approach to model the curing process in magneto-sensitive polymeric materials. International Journal of Solids and Structures 69–70, 34–44.

Hu, W., Zhan, G., Mastrangeli, M., Sitti, M., 2018. Small-scale soft-bodied robot with multimodal locomotion. Nature 554, 81–85.

Ivaneyko, D., Toshchevikov, V.P., Saphiannikova, M., Heinrich, G., 2011. Magneto-sensitive elastomers in a homogeneous magnetic field: a regular rectangular lattice model. Macromolecular Theory and Simulations 20, 411–424.

Ivaneyko, D., Toshchevikov, V., Saphiannikova, M., Heinrich, G., 2012. Effects of particle distribution on mechanical properties of magneto-sensitive elastomers in a homogeneous magnetic field. Condensed Matter Physics 15, 33601.

Ivaneyko, D., Toshchevikov, V., Saphiannikova, M., Heinrich, G., 2014. Mechanical properties of magneto-sensitive elastomers: unification of the continuum-mechanics and microscopic theoretical approaches. Soft Matter 10 (13), 2213–2225.

Jolly, M.R., Carlson, J.D., Muñoz, B.C., 1996. A model of the behaviour of magnetorheological materials. Smart Materials and Structures 5, 607–614.

Kadapa, C., Hossain, M., 2020. A linearised consistent mixed displacement-pressure formulation for hyperelasticity. Mechanics of Advanced Materials and Structures. https://doi.org/10.1080/15376494.2020.1762952 (in press).

Kallio, M., 2005. The elastic and damping properties of magnetorheological elastomers. VTT Publications 565.

Kankanala, S.V., Triantafyllidis, N., 2004. On finitely strained magnetorheological elastomers. Journal of the Mechanics and Physics of Solids 52, 2869–2908.

Keip, M.-A., Sridhar, A., 2019. A variationally consistent phase-field approach for micro-magnetic domain evolution at finite deformations. Journal of the Mechanics and Physics of Solids 125, 805–824.

Khanouki, M.A., Sedaghati, R., Hemmatian, M., 2019. Experimental characterization and microscale modeling of isotropic and anisotropic magnetorheological elastomers. Composites B: Engineering 176, 107311.
Kim, Y., Yuk, H., Zhao, R., Chester, S.A., Zhao, X., 2018. Printing ferromagnetic domains for untethered fast-transforming soft materials. Nature 558 (7709), 274–327.
Kovetz, A., 2000. Electromagnetic Theory. University Press, Oxford.
Lee, E.H., 1969. Elastic-plastic deformation at finite strains. Journal of Applied Mechanics 36, 1–6.
Liao, Z., Hossain, M., Yao, H., 2020. Ecoflex polymer of different Shore hardnesses: experimental investigations and constitutive modelling. Mechanics of Materials 144 (103366), 2020.
Lopez-Pamies, O., 2010. A new I1-based hyperelastic model for rubber elastic materials. Comptes Rendus Mecanique 338, 3–11.
Lu, H., Xing, Z., Hossain, M., Fu, Y.Q., 2019. Modeling strategy for dynamic-modal mechanophore in double-network hydrogel composites with self-growing and tailorable mechanical strength. Composites Part B: Engineering 179, 107528.
Martin, E.J., Anderson, R.A., Read, D., Gerald Gulley, G., 2006. Magnetostriction of field-structured magnetoelastomers. Physical Review E 74, 051507.
Maugin, G.A., 1988. Continuum Mechanics of Electromagnetic Solids. North Holland, Amsterdam.
Mehnert, M., Hossain, M., Steinmann, P., 2017. Towards a thermo-magneto-mechanical coupling framework for magneto-rheological elastomers. International Journal of Solids and Structures 128, 117–132.
Miehe, C., Göktepe, S., Lulei, F., 2004. A micro-macro approach to rubber-like materials-Part I: the non-affine micro-sphere model of rubber elasticity. Journal of the Mechanics and Physics of Solids 52, 2617–2660.
Mukherjee, D., Bodelot, L., Danas, K., 2020. Microstructurally-guided explicit continuum models for isotropic magnetorheological elastomers with iron particles. International Journal of Non-Linear Mechanics 120, 103380.
Nedjar, B., 2019. A modelling framework for finite strain magnetoviscoelasticity. Mathematics and Mechanics of Solids 25 (2), 288–304.
Pao U.H., 1978. Electromagnetic forces in deformable continua. In: Nemat-Nasser, S. (Ed.), Mechanics Today, vol. 4, Oxford University Press, pp. 209–305..
Pelteret, J.P., Walter, B., Steinmann, P., 2018. Application of metaheuristic algorithms to the identification of nonlinear magneto-viscoelastic constitutive parameters. Journal of Magnetism and Magnetic Materials 464, 116–131.
Ren, Z., Hu, W., Dong, X., Sitti, M., 2019. Multi-functional soft-bodied jellyfish-like swimming. Nature Communications 10, 2703.
Saxena, P., Hossain, M., Steinmann, P., 2013. A theory of finite deformation magneto-viscoelasticity. International Journal of Solids and Structures 50 (24), 3886–3897.
Saxena, P., Hossain, H., Steinmann, P., 2014. Nonlinear magneto-viscoelasticity of transversally isotropic magneto-active polymers. Proceedings of the Royal Society of London. Series A 470, 20140082.
Schubert, G., Harrison, P., 2015. Large-strain behaviour of magneto-rheological elastomers tested under uniaxial compression and tension, and pure shear deformations. Polymer Testing 42, 122–134.
Schubert, G., Harrison, P., 2015. Equi-biaxial tension tests on magneto-rheological elastomers. Smart Materials and Structures 25, (1) 015015.
Shariff, M.H.B.M, Bustamante, R., Hossain, M., Steinmann, P., 2016. A novel spectral formulation for transversely isotropic magneto-elasticity. Mathematics and Mechanics of Solids (in Press)..
Soria-Hernandez, C.G., Palacios-Pineda, L.M., Elias-Zuniga, A., Perales-Martinez, I.A., Martinez-Romero, O., 2019. Investigation of the effect of carbonyl iron micro-particles on the mechanical and rheological properties of isotropic and anisotropic MREs: constitutive magneto-mechanical material model. Polymers 11 (10), 1705.
Steinmann, P., Hossain, M., Possart, G., 2012. Hyperelastic models for rubber-like materials: consistent tangent operators and suitability of Treloar's data. Archive of Applied Mechanics 82 (9), 1183–1217.
Stepanov, G.V., Abramchuk, S.S., Grishin, D.A., Nikitin, L.V., Kramarenko, E.Y., Khokhlov, A.R., 2007. Effect of a homogeneous magnetic field on the viscoelastic behavior of magnetic elastomers. Polymer 48 (2), 488–495.
Varga, Z., Filipcsei, G., Zrínyi, M., 2006. Magnetic field sensitive functional elastomers with tuneable modulus. Polymer 47, 227–233.
Zabihyan, R., Mergheim, J., Pelteret, J.P., Brands, B., Steinmann, P., 2020. FE2 simulations of magnetorheological elastomers: influence of microscopic boundary conditions, microstructures and free space on the macroscopic responses of MREs. International Journal of Solids and Structures 193–194, 338–356.
Zhao, R., Kim, Y., Chester, A.S., Sharma, P., Zhao, X., 2019. Mechanics of hard-magnetic soft materials. Journal of the Mechanics and Physics of Solids 124, 244–263.
Zhou, G.Y., Jiang, Z.Y., 2004. Deformation in magnetorheological elastomer and elastomer-ferromagnet composite driven by a magnetic field. Smart Materials and Structures 13, 309.